Accuracy of Density Functional Theory for Predicting Kinetics of Methanol Synthesis from CO and CO_2 Hydrogenation on Copper

Maliheh Shaban Tameh,[†] Albert K. Dearden,[†] and Chen Huang[*,‡]

[†]*Department of Scientific Computing, Florida State University, Tallahassee, Florida 32306, USA*

[‡]*Department of Scientific Computing and National High Magnetic Field Laboratory, Florida State University, Tallahassee, Florida 32306, USA*

E-mail: chuang3@fsu.edu

Abstract

Density functional theory (DFT) is widely used for investigating heterogeneous catalysis; however, the predictive power of DFT is determined by the approximation used in the exchange-correlation (XC) functionals. In this work, we systematically investigate how the kinetics of methanol synthesis predicted by DFT depends on the choice of XC functionals. Microkinetic modelings are performed based on the Gibbs energies calculated with XC functionals that represent three levels of accuracy: Perdew-Burke-Ernzerhof (PBE) functional, Heyd-Scuseria-Ernzerhof (HSE) hybrid functional, and the random phase approximation (RPA) functional. We show that the predicted kinetics strongly depends on the choice of XC functionals. Methanol's turnover frequencies predicted by PBE and HSE are about 30 times faster than the predictions from RPA. PBE predicts that the overall barrier of CO hydrogenation is 0.56 eV lower than that of CO_2 hydrogenation, therefore suggesting CO as the carbon source for methanol synthesis on copper. This contradicts previous isotope-labeling experiments that supported CO_2 as the carbon source in industrial methanol synthesis; therefore, PBE suggests that metallic copper cannot be the active site for CO_2 hydrogenation. On the other hand, the overall barrier of CO hydrogenation, predicted by HSE and RPA, is lower than the overall barrier of CO_2 hydrogenation by 0.22 eV and 0.14 eV, respectively. This suggests that CO_2 hydrogenation is also competitive for methanol production, and we cannot completely rule out the possibility that metallic copper is the active site for catalyzing CO_2 hydrogenation. In addition, the prediction of the dominating adsorbates also strongly depends on the choice of XC functionals. Our results show that different XC functionals can predict different kinetics for methanol synthesis, which calls attention to the accuracy of DFT for modeling methanol synthesis.

1 Introduction

Methanol is an important building block for synthesizing many chemicals, and is used as the fuel for combustion engines and the direct methanol fuel cells. Methanol is synthesized through CO and CO_2 hydrogenations. Low pressure methanol synthesis is performed with the Cu/ZnO catalyst system.[1] The catalytic process involves many competing processes such as CO hydrogenation, CO_2 hydrogenation, and the water-gas shift reaction. These processes are coupled. In addition, the morphology of the catalysts can change in response to different adsorbates.[2] Due to such complexity, the mechanism of methanol synthesis is under extensive debate.

A long-term effort is to identify the active sites. Metallic copper has long been proposed as the active site,[1,3–17] and oxides are added to maintain large copper surface and to reduce CuO to metallic copper.[18–21] Others suggested that methanol is synthesized over Cu^+ at Cu/ZnO interface,[22–25] or over the Cu cations that dissolve in ZnO matrix,[26,27] and suggested that metallic copper only promotes the dissociation of H_2.[26,28–30]

Without pinning down the active sites, it is difficult to resolve another related puzzle: what the carbon source is in industrial methanol synthesis. It was suggested that methanol was mainly produced through CO hydrogenation,[31–33] and the role of CO_2 was to maintain the oxidation state of copper and the dispersion of copper particles.[30,34,35] This supports the argument that oxidized copper is the active site. Others suggested that CO and CO_2 play equal roles,[36–39] and CO and CO_2 hydrogenations take place at different active sites.[40–42] CO_2 has also been proposed to be the major carbon source.[1,40,43–47] The role of CO was suggested to maintain the reduced state of copper for CO_2 hydrogenation[1] or to inhibit the reverse water-gas shift reaction that consumes CO_2.[48,49] Evidences from isotope-labeling experiments[44,47,50,51] strongly support that CO_2 is the major carbon source in methanol synthesis performed over the industrial catalysts.

Density functional theory (DFT)[52,53] can help us resolve these puzzles by, for example, screening candidate active sites. Unfortunately, the predictive power of DFT is hindered

by the approximated exchange-correlation (XC) functionals. For example, the generalized gradient approximated (GGA) functional is known to overestimate the adsorption energies of molecules on transition metals.[54,55] For methanol synthesis on copper, previous DFT-GGA calculations[39,56] predicted that the overall barrier of CO hydrogenation is lower than the overall barrier of CO_2 hydrogenation, which contradicts the isotope-labeling experiments that suggested CO_2 as the major carbon source. This discrepancy between DFT and experiments can be due to three reasons: (1) metallic copper is not the active site for CO_2 hydrogenation in industrial methanol synthesis, (2) the isotope-labeling experiments were misinterpreted, and (3) DFT-GGA gave inaccurate energetics for CO and CO_2 hydrogenation on copper. In this work, we examine the last possible reason.

The question that whether the relatively low overall barrier of CO hydrogenation predicted by GGA is due to GGA's error was recently investigated by Studt and coworkers.[57] By using the BEEF-vdW functional,[58] they found that the energies of most intermediates in the CO_2 pathway were lowered. For the CO pathway, BEEF-vdW functional did not have significant correction. As a result, the overall barrier of CO_2 pathway became comparable to the overall barrier of the CO pathway. The improved energetics were attributed to two reasons: (a) the inclusion of the van der Waals (vdW) interaction in BEEF-vdW functional, and (b) more accurate bonding energies between adsorbates and copper predicted by BEEF-vdW functional.[57] Microkinetic modeling based on their BEEF-vdW energies were later carried out,[59] which predicted that CO_2 was the major carbon source. The error of GGA functionals was also investigated by Peterson et al..[60] They corrected the energies of the molecules and radicals that contain OCO backbones. In the work of Grabow and Mavrikakis,[39] they lowered the GGA energies of several key intermediates by 0.3$\sim$0.6 eV to better reproduce the experiment results.

In this work, we examine CO and CO_2 hydrogenations on copper using the exact exchange (EXX) and the direct random phase approximation (RPA) correlation functional[61–68] (in which the exchange-correlation kernel is zero). The accuracy of RPA for describing surface

reactions has been assessed recently. RPA provides a reasonable description of the vdW interaction and significantly improved the adsorption energies of CO on transition metals.[69] In the study of water splitting over an iron atom, the RPA predictions agreed well with the coupled cluster method.[70] However, we address that RPA does not always reach the chemical accuracy (1 kcal/mol) for transition metal chemistry, as demonstrated in Ref.[71], in which a detailed comparison between RPA and many other types of XC functionals was performed in the context of investigating water splitting over an iron atom.[71] RPA gave more accurate predictions for the reaction barriers than most GGA functionals, but gave poorer predictions for the reaction energies.[71] Therefore, at the end of this work, we assess the RPA's accuracy for predicting the energies of methanol synthesis over copper.

The paper is organized as follows. We first investigate the accuracy of different XC functionals for predicting the thermodynamics of CO and CO_2 hydrogenation. We construct the Gibbs energy diagrams of CO and CO_2 hydrogenation on copper using Perdew-Burke-Ernzerhof (PBE)[72] functional, Heyd-Scuseria-Ernzerhof (HSE) 2006[73,74] hybrid functional, and EXX and RPA correlation functional. Microkinetic modeling[75] is performed to investigate how the predicted kinetics of CO and CO_2 hydrogenation depends on the choice of XC functionals, which is further explained by solving the microkinetic models analytically. We show that the prediction of the major carbon source strongly depends on the choice of XC functionals. In the end, we examine the accuracy of RPA by computing enthalpies of selected molecules and radicals on Pt(111).

2 Computational details

To investigate the accuracy of different XC functionals for predicting the thermodynamics of CO and CO_2 hydrogenations, we define the Gibbs energy changes of CO and CO_2

hydrogenation as

$$\Delta G_{\mathrm{CO}} = G_{\mathrm{H_3COH}} - G_{\mathrm{CO}} - 2G_{\mathrm{H_2}} \tag{1}$$

$$\Delta G_{\mathrm{CO_2}} = G_{\mathrm{H_3COH}} + G_{\mathrm{H_2}O} - G_{\mathrm{CO_2}} - 3G_{\mathrm{H_2}}, \tag{2}$$

where G_{X} is the Gibbs energy of molecule X at 500 K and the corresponding partial pressures. In this work, the partial pressures of CO, CO_2, H_2, H_3COH, and H_2O are 10 bar, 10 bar, 40 bar, 1 bar, and 1 bar, respectively. For molecule X, its Gibbs energy is obtained as $G_{\mathrm{X}} = E_{\mathrm{X}}^{\mathrm{DFT}} + \Delta G_{\mathrm{X}}$. ΔG_{X} is the thermal correction to Gibbs energy and is calculated using Gaussian 09 program[76] using PBE functional at 500 K and the partial pressure of molecule X. $E_{\mathrm{X}}^{\mathrm{DFT}}$ is the DFT energy calculated using different levels of XC functionals, including five GGA functional (PBE, PW91,[77] RPBE,[54] BEEF-vdW, and HLE16[78]), five meta-GGA functionals (Tao-Perdew-Staroverov-Scuseria (TPSS),[79] revTPSS,[80,81] the strongly constrained and appropriately normed (SCAN) functional,[82] HLE17,[83] and M06-L[84]), three hybrid functionals (PBE0,[85] HSE, and B3LYP[86]), and EXX+RPA. These calculations are performed using the Vienna Ab-initio Simulation Package (VASP),[87–91] except HLE16 and HLE17 functionals which are calculated using Gaussian 09 program with cc-pVQZ basis sets.[92] Hybrid calculations are performed with a kinetic energy cutoff of 400 eV. RPA calculations are performed with a kinetic energy cutoff of 300 eV. In VASP calculations, the molecules are put in $10 \times 10 \times 10$ Å cells.

ΔG_{CO} and $\Delta G_{\mathrm{CO_2}}$ predicted by different XC functionals are compared to the references. To obtain the references, the Gibbs energy of molecule X is calculated as $G_{\mathrm{X}}^{\mathrm{Ref}} = \Delta_{\mathrm{f}} H^{o}_{\mathrm{gas,X}} - \Delta H_{\mathrm{X}}^{\mathrm{DFT}} + \Delta G_{\mathrm{X}}^{\mathrm{DFT}}$. $\Delta_{\mathrm{f}} H^{o}_{\mathrm{gas,X}}$ is the molecule X's standard enthalpy of formation, taken from NIST Chemistry WebBook[93] (with the specific references given later). $\Delta_{\mathrm{f}} H^{o}_{\mathrm{gas,X}}$ is -1.14 eV,[94] -4.07 eV,[94] 0.0 eV, -2.51 eV,[94] and -2.12 eV[93] for gas-phase CO, CO_2, H_2, H_2O, and H_3COH, respectively. $\Delta H_{\mathrm{X}}^{\mathrm{DFT}}$ is the thermal correction to enthalpy at the standard conditions. $\Delta G_{\mathrm{X}}^{\mathrm{DFT}}$ is the correction to Gibbs energy, calculated at 500 K and the molecule

X's partial pressure. Both $\Delta H_{\mathrm{X}}^{\mathrm{DFT}}$ and $\Delta G_{\mathrm{X}}^{\mathrm{DFT}}$ are computed using Gaussian 09 program with PBE functional and cc-pVQZ basis set.

To model CO and CO_2 hydrogenations on copper, a copper face-centered cubic (FCC) (211) surface is employed to represent surface defects and is modeled by a 3×3 super-cell and a four-layer slab separated from its periodic image by a 10 Å vacuum. Structures are relaxed using the Quantum Espresso program[95] with PBE functional and a kinetic energy cutoff of 550 eV. Top two Cu layers and adsorbates are free to move. Fermi-Dirac smearing with a smearing temperature of 0.1 eV is used. A $4\times4\times1$ Monkhorst-Pack[96] k-point mesh is used. Transition states are identified using the string method.[97,98] To reduce the computational cost, images are relaxed with all Cu atoms kept fixed and a smaller $2\times2\times1$ k-point mesh.

To model Pt FCC(111) surface, a 3×3 unit cell with a five-layer slab is used. A 10 Å vacuum is added to reduce the interaction between the periodic images. Structures are relaxed with the bottom three Pt layers kept fixed, and are relaxed using VASP with a kinetic energy cutoff of 500 eV and a k-point mesh of $6\times6\times1$. Gaussian smearing with a smearing temperature of 0.1 eV is used. Transition states are identified using the nudged elastic band (NEB) theory.[99–102]

The ONIOM method[103] is used to obtain the adsorption energies with HSE and RPA accuracies. With ONOIM, the system's energy is defined as

$$E^{\mathrm{ONIOM}} = E_{\mathrm{total}}^{\mathrm{low}} + (E_{\mathrm{cluster}}^{\mathrm{high}} - E_{\mathrm{cluster}}^{\mathrm{low}}), \tag{3}$$

where PBE is considered as the low-level method in this work. $E_{\mathrm{total}}^{\mathrm{low}}$ and $E_{\mathrm{cluster}}^{\mathrm{low}}$ are the system and cluster's PBE energies. For methanol synthesis over Cu(211), $E_{\mathrm{total}}^{\mathrm{low}}$ is calculated with a kinetic energy cutoff of 400 eV and k-point mesh of $4\times4\times1$. In the study of the adsorption energies of molecules and radical on Pt(111) surface, $E_{\mathrm{total}}^{\mathrm{low}}$ is calculated with a kinetic energy cutoff of 400 eV and a k-point mesh of $6\times6\times1$. In Eq. 3, $E_{\mathrm{cluster}}^{\mathrm{high}}$ is the cluster's high-level energy calculated using either HSE or RPA. The top three metal (Cu or Pt) layers

and the adsorbates are selected to be the clusters. The clusters are chosen to be large enough to include the interaction between adsorbates and metal surfaces. Clusters' HSE and RPA calculations are performed with VASP using a reduced kinetic energy cutoff of 300 eV and a reduced k-point mesh of $2 \times 2 \times 1$ to lower the computational cost. The costs of the RPA and HSE calculations are further reduced by reducing the cell sizes in the z direction while still keeping the periodic images separated by a 10 Å vacuum. The same settings are used to calculate $E^{\text{low}}_{\text{cluster}}$ to achieve the error cancellation between $E^{\text{low}}_{\text{cluster}}$ and $E^{\text{high}}_{\text{cluster}}$. The integral over the frequency in RPA correlation energy is evaluated using 16 frequency points.[104] In Supporting Information, we tested the convergence of RPA calculations with respect to different settings of kinetic energy cutoffs, k-point meshes, cell sizes in z direction, and the numbers of copper layers included in clusters. We find that the Gibbs energy difference between H-HCO/Cu(211) and H-HCOOH/Cu(211) can be reasonably predicted with the above low settings.

Gibbs energies and enthalpies of adsorbates on Cu(211) and Pt(111) are calculated by only considering the vibrational contributions from the adsorbates. The vibrational frequencies are obtained by diagonalizing the Hessian matrices that are built using the central finite difference method with the substrate metal atoms kept fixed.

For surface reactions, the rate constants are calculated according to the transition state theory

$$k = \frac{k_B T}{h} e^{-\Delta G_a / k_B T}, \tag{4}$$

where ΔG_a is forward or reverse Gibbs reaction barriers. k_B and h are Boltzmann constant and Planck constant, respectively. T is 500 K in this work.

The kinetics of CO and CO_2 hydrogenation is studied with microkinetic modeling, under the assumption that the adsoprtion energies are independent of the coverage and the distribution of adsorbates are homogeneous. The elementary steps of CO and CO_2 hydrogenations on Cu(211) are listed in Table 1. The coverages of CO*, H*, H_3COH*, CO_2*, and H_2O* are calculated by assuming that the adsorption processes are at quasi-equilibrium.[105,106] For

example, the coverage of CO* is calculated as $\theta_{\mathrm{CO}} = K_1\theta_*$ where θ_* is the percentage of the free surface and

$$K_1 = e^{-(G_{\mathrm{CO}*} - G_{\mathrm{CO(g)}})/k_B T}$$

is the equilibrium constant of the CO adsorption (reaction 1 in Table 1), with $G_{\mathrm{CO}*}$ and $G_{\mathrm{CO(g)}}$ being the Gibbs energies of adsorbed CO and gas-phase CO, respectively. The rate equations used for microkinetic modeling are given in the Supporting Information and are integrated using MATLAB[107] until the steady states are reached.

The turnover frequency (TOF) of methanol, R, is given by the rate of reaction 6 in Table 1

$$R = k_6^+ \theta_{\mathrm{H_3CO}} \theta_{\mathrm{H}} - k_6^- \theta_{\mathrm{H_3COH}} \theta_*, \tag{5}$$

where k_6^+ and k_6^- are the forward and reverse rate constants of reaction 6. The rate-limiting steps are determined by calculating the degree of rate control[108] of all reaction steps. For the step i, it is

$$X_{RC,i} = \frac{k_i}{R} \left(\frac{\partial R}{\partial k_i} \right)_{\{K_i, k_{j\neq i}\}} \tag{6}$$

where $\{k_{j\neq i}\}$ are the rate constants of other reaction steps rather than the step i. K_i is the equilibrium constant of the step i. The derivative $\partial R/\partial k_i$ is taken with $\{k_{j\neq i}\}$ and K_i kept constant.

3 Results and discussions

3.1 Thermodynamics of CO and CO_2 hydrogenation predicted by XC functionals of different levels

We investigate the accuracy of XC functionals for predicting the Gibbs energies of CO and CO_2 hydrogenations (ΔG_{CO} and $\Delta G_{\mathrm{CO_2}}$ defined in Eqs. 1 and 2). It is important

Table 1: Elementary reaction steps for CO and CO_2 hydrogenation on Cu(211). "*" indicates free surface. Gas-phase molecules are denoted by "(g)".

CO hydrogenation:	
1	$CO(g) + * \rightarrow CO*$
2	$H_2(g) + 2* \rightarrow 2H*$
3	$CO* + H* \rightarrow HCO* + *$
4	$HCO* + H* \rightarrow H_2CO* + *$
5	$H_2CO* + H* \rightarrow H_3CO* + *$
6	$H_3CO* + H* \rightarrow H_3COH* + *$
7	$H_3COH* \rightarrow H_3COH(g) + *$
CO_2 hydrogenation:	
8	$CO_2(g) + * \rightarrow CO_2*$
2	$H_2(g) + 2* \rightarrow 2H*$
9	$CO_2* + H* \rightarrow HCOO* + *$
10	$HCOO* + H* \rightarrow HCOOH* + *$
11	$HCOOH* + H* \rightarrow H_2COOH* + *$
12	$H_2COOH* + * \rightarrow H_2CO* + OH*$
5	$H_2CO* + H* \rightarrow H_3CO* + *$
6	$H_3CO* + H* \rightarrow H_3COH* + *$
7	$H_3COH* \rightarrow H_3COH(g) + *$
13	$OH* + H* \rightarrow H_2O* + *$
14	$H_2O* \rightarrow H_2O(g) + *$

to accurately predict ΔG_{CO} and ΔG_{CO_2}, since they determine whether the hydrogenation reactions proceed spontaneously. Four different levels of XC functionals are studied: GGA, meta-GGA, hybrid, and RPA. The results are given in Fig. 1.

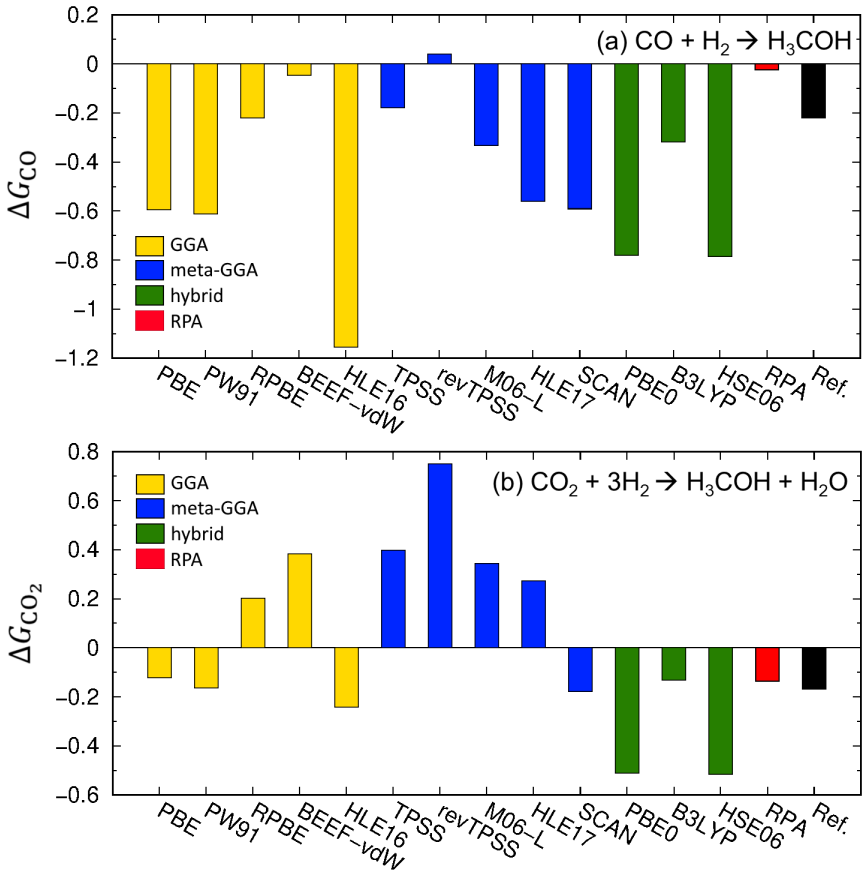

Figure 1: The change of Gibbs energies of (a) CO and (b) CO_2 hydrogenations calculated by GGA, meta-GGA, hybrid, and RPA functionals at 500 K. The pressures for CO, CO_2, H_2, H_3COH, and H_2O are 10 bar, 10 bar, 40 bar, 1 bar, and 1 bar, respectively. The references are denoted by "Ref.". The energies are in eV.

For GGA functionals, PBE and PW91 give reasonable predictions to ΔG_{CO_2}, but significantly overestimate ΔG_{CO}. RPBE[54] and BEEF-vdW functionals predict that CO_2 hydrogenation is not thermodynamically favorable, which is due to their errors in treating the OCO backbone.[57,60] HLE16 gives reasonable prediction to ΔG_{CO_2}, but much overestimates ΔG_{CO}. All meta-GGA functionals, except SCAN, predict that CO_2 hydrogenation is not thermodynamically favorable. In addition, revTPSS predicts that CO hydrogenation is not

thermodynamically favorable. Therefore, in the following section we only report results from SCAN functional. For hybrid functionals, the performance of PBE0 and HSE are similar and they both significantly overestimate the Gibbs energies of CO and CO_2 hydrogenations. B3LYP has a better performance: It slightly overestimates CO hydrogenation and slightly underestimates CO_2 hydrogenation. However B3LYP cannot be used in following studies of methanol synthesis over Cu(211), since it contains a fraction of Hartree-Fock exchange and cannot be applied to metals. In the following discussions, HSE functional is employed. For RPA, it well reproduces ΔG_{CO_2}, but severely underestimates ΔG_{CO}.

3.2 Gibbs energetics of CO and CO_2 hydrogenation on Cu(211)

Fig. 2 gives the Gibbs energies calculated using PBE, SCAN, HSE, and RPA. To obtain a correct prediction of the fastest hydrogenation pathway, an XC functional needs to have similar errors for gas-phase CO, CO_2, H_2, H_2O, H_3COH, and all the intermediates in Fig. 2 to achieve good error cancellations among them. This means that the PBE, SCAN, HSE, and RPA energy diagrams should overlap, which, however, is not observed in Fig. 2. This indicates that not all (or none) of these XC functionals have the desired error cancellation.

The fastest hydrogenation pathway is mainly determined by the Gibbs energy difference between H-HCO* and H-HCOOH* (denoted as ΔG_{RLS}). H-HCO* and H-HCOOH* are the transition states of the rate-limiting steps of the CO and CO_2 hydrogenation, respectively, as determined later with microkinetic modeling. PBE promotes CO hydrogenation by predicting that the Gibbs energy of H-HCO* is 0.56 eV lower than H-HCOOH*, that is, $\Delta G_{RLS} = 0.56$ eV. HSE and RPA much reduce ΔG_{RLS}, and predict ΔG_{RLS} to be 0.22 eV and 0.14 eV, respectively. Therefore, RPA suggests that CO_2 pathway is competitive.

In general, Gibbs energies predicted by SCAN are much lower than the predictions from PBE, HSE, and RPA. It is known that PBE overestimates the binding energy between CO and copper surface (the so-called "CO puzzle").[55,109,110] Fig. 2(a) shows that SCAN overestimates the binding energy more. Therefore, in the following discussions, we focus on

PBE, HSE, and RPA functionals.

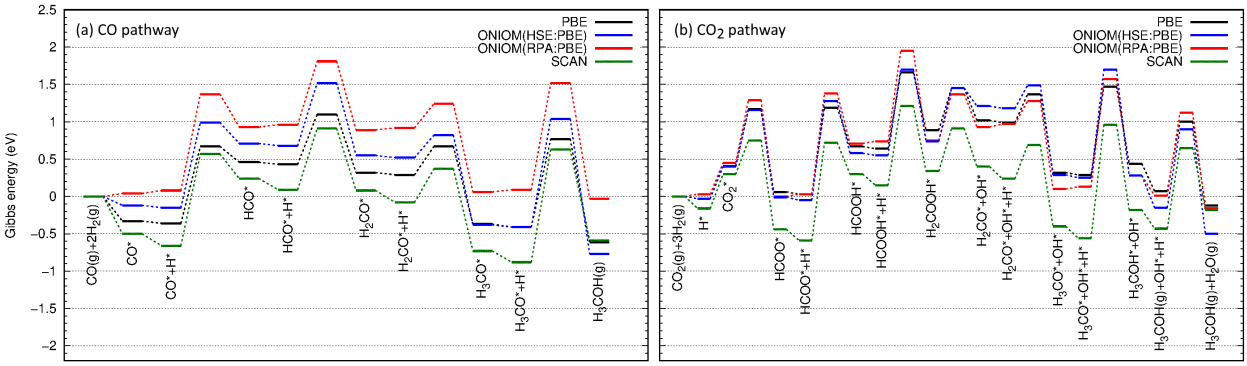

Figure 2: Gibbs energies for (a) CO and (b) CO_2 hydrogenation on Cu(211), calculated with PBE, SCAN, ONIOM(HSE:PBE), and ONIOM(RPA:PBE). For CO pathway, the energies are referenced to CO(g) and H_2(g). For CO_2 pathway, the energies are referenced to CO_2(g) and H_2(g).

3.3 Kinetics of CO and CO_2 hydrogenation on copper using XC functionals of different levels of accuracy

To examine how the predicted kinetics of CO and CO_2 hydrogenation depends on the choice XC functionals, we perform microkinetic modeling on each hydrogenation pathway. For CO hydrogenation, PBE, HSE, and RPA all predict HCO* + H* $\rightarrow$ H_2CO to be the rate-limiting step with $X_{RC} = 0.99$. For CO_2 hydrogenation, they predict that the rate-limiting step is HCOOH* + H* $\rightarrow$ H_2COOH* with $X_{RC} = 0.99$. We note that these rate-limiting steps are the transition states with the highest Gibbs energies in Fig. 2, which is due to the fact that all the other reaction steps are at quasi-equilibrium, as validated later by solving the microkinetic models analytically.

Fig. 3 shows that the coverages of the intermediates depend on the choice of XC functionals. For CO hydrogenation, PBE predicts that the surface is nearly fully occupied by CO* with a coverage of 99.7%. This is consistent with the observation in Fig. 2(a) that CO* is predicted by PBE to have the lowest free energy among all the intermediates before the rate-limiting step. Even though PBE predicts that H_3CO* has a lower Gibbs energy

than CO*, the coverage of H_3CO* predicted by PBE is nearly zero. The reason is that H_3CO* is after the rate-limiting step, and therefore is at quasi-equilibrium with H_3COH(g). Since H_3CO* has a higher Gibbs energy than H_3COH(g), H_3CO* is quickly hydrogenated to H_3COH(g), once it is produced. With HSE and RPA, CO's coverage is much reduced, because the overbinding problem of CO on copper is much alleviated by HSE and RPA. The coverages of CO* and H* predicted by RPA are 20.0% and 24.1%, respectively. The reason for a large coverage for H* is that the Gibbs energy of H* predicted by RPA is 0.01 eV lower than that of CO*. RPA also predicts a large free surface (52.5%). The HSE prediction is roughly between PBE and RPA: CO* (84.2%) and H* (10.4%).

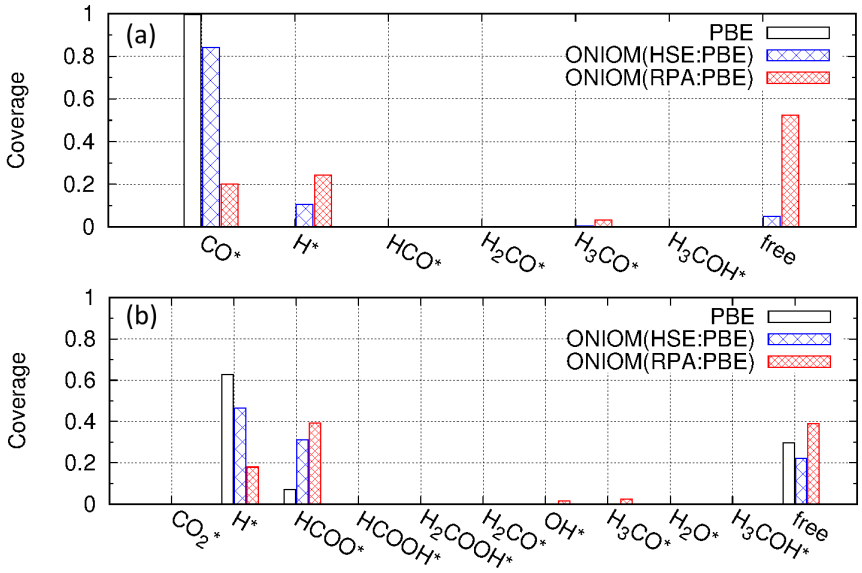

Figure 3: Coverages of the intermediates in the (a) CO and (b) CO_2 hydrogenation by solving microkinetic models based on the energetics from PBE, ONIOM(HSE:PBE), and ONIOM(RPA:PBE) calculations. The amount of free surface is denoted by "free".

For CO_2 hydrogenation, PBE predicts H* to be the major intermediate on surface with a coverage of 62.8%. PBE predicts a small coverage for HCOO* (7.2%), and 29.7% free surface. Again, RPA gives different results. It predicts that the surface is largely occupied by HCOO* with a coverage of 39.1%. This is consistent with the RPA Gibbs energies in Fig. 2(b) which shows that HCOO* has the lowest Gibbs energy among all the intermediates before the rate-limiting step. The HSE predictions for the coverages of H* and HCOO* is,

again, between PBE and RPA.

3.4 Understand the kinetics of CO and CO_2 hydrogenation based on the analytical solutions to the microkinetic models

In Table 2, we find that TOFs also much depend on the choice of XC functionals. For example, RPA TOFs are much smaller than PBE and HSE TOFs. One puzzle is that PBE and HSE give similar TOFs to the CO pathway, which seems contradictory to the observation in Fig. 2(a) that HSE predicts a much higher overall barrier for the CO hydrogenation.

To explain these observations, we solved the microkinetic models analytically by assuming that all the reaction steps in Table 1 are at quasi-equilibrium except the rate-limiting steps (reactions 4 and 11). For a reaction step at quasi-equilibrium, the coverages of its reactants and products are related by the equilibrium constant of that reaction.[106,111] These assumptions are validated by the good agreement between the analytical solutions to the TOFs and the TOFs obtained by numerically integrating the rate equations, as shown in Table 2. This good agreement is, in fact, expected, since the degrees of rate control of these rate-limiting steps are close to 100%.

Table 2: Methanol TOFs (s^{-1}) for CO and CO_2 pathways based on the energies from PBE, ONIOM(HSE:PBE), and ONIOM(RPA:PBE) calculations. The TOFs (s^{-1}) obtained by solving the microkinetic models analytically are given in the parentheses.

	PBE	HSE	RPA
CO pathway	1.84×10^{-5}	1.37×10^{-5}	1.35×10^{-6}
	(1.85×10^{-5})	(1.38×10^{-5})	(1.36×10^{-6})
CO_2 pathway	1.60×10^{-5}	3.86×10^{-6}	3.82×10^{-8}
	(1.61×10^{-5})	(3.87×10^{-6})	(3.82×10^{-8})

For the CO pathway, the analytical solution for methanol's TOF is

$$R_{\mathrm{CO}}^{\mathrm{analytical}} = k_4^+ K_{\mathrm{R,CO}} \theta_*^2 - k_4^- K_{\mathrm{P,CO}} \theta_*^2, \tag{7}$$

where $r_{\mathrm{CO}}^+ = k_4^+ K_{\mathrm{R,CO}} \theta_*^2$ and $r_{\mathrm{CO}}^- = k_4^- K_{\mathrm{P,CO}} \theta_*^2$ are the forward and reverse rates of the

rate-limiting step (reaction 4 in Table 1). $K_{\mathrm{R,CO}} = K_1K_2K_3$ is the equilibrium constant of the overall reaction CO(g) + H_2(g) + 2* $\rightarrow$ HCO* + H*, which combines reactions 1, 2, and 3 in Table 1. $K_{\mathrm{P,CO}} = 1/(K_5K_6K_7K_2)$ is the equilibrium constant of the overall reaction H_3COH(g) + * $\rightarrow$ H_2(g) + H_2CO* which combines reactions 2, 5, 6, and 7. Since the intermediates before the rate-limiting step are at quasi-equilibrium, we have $K_{\mathrm{R,CO}}\theta_*^2 = \theta_{\mathrm{HCO}}\theta_{\mathrm{H}}$. Similarly, we have $K_{\mathrm{P,CO}}\theta_*^2 = \theta_{\mathrm{H_3COH}}\theta_*$. A larger $K_{\mathrm{R,CO}}$ ($K_{\mathrm{P,CO}}$) increases the coverages of HCO* and H* (H_2CO*), therefore promoting the forward (reverse) reaction of the rate-limiting step. The free surface θ_* is

$$\begin{aligned}\theta_*^{-1} &= K_1 + \sqrt{K_2} + \sqrt{K_2}K_1K_3 \\ &\quad + \frac{1}{K_2K_5K_6K_7} + \frac{1}{K_6K_7K_2} + \frac{1}{K_7} + 1. \end{aligned} \tag{8}$$

For the CO_2 pathway, the TOF of methanol is the difference between the forward and reverse rates of the rate-limiting step (reaction 11 in Table 1)

$$R_{\mathrm{CO_2}}^{\mathrm{analytical}} = k_{11}^{+}K_{\mathrm{R,CO_2}}\theta_*^2 - k_{11}^{-}K_{\mathrm{P,CO_2}}\theta_*^2, \tag{9}$$

where $K_{\mathrm{R,CO_2}} = K_2^{3/2}K_8K_9K_{10}$ and $K_{\mathrm{P,CO_2}} = 1/(K_2^{3/2}K_{12}K_{13}K_5K_6K_7K_{14})$ give the equilibrium constants of the overall reaction CO_2(g) + 3/2H_2(g) + 2* $\rightarrow$ HCOOH* + H* and the overall reaction H_3COH(g) + H_2O(g) + * $\rightarrow$ H_2COOH* + 3/2H_2(g), respectively. The free surface θ_* is

$$\begin{aligned}\theta_*^{-1} &= K_8 + \sqrt{K_2} + K_8\sqrt{K_2}K_9 + K_8K_2K_9K_{10} \\ &\quad + \frac{1}{K_7} + \frac{1}{K_{14}} + \frac{1}{\sqrt{K_2}K_6K_7} \\ &\quad + \frac{1}{\sqrt{K_2}K_{13}K_{14}} + \frac{1}{K_2K_5K_6K_7} \\ &\quad + \frac{1}{K_2^{3/2}K_{12}K_{13}K_5K_6K_7K_{14}} + 1. \end{aligned} \tag{10}$$

Above analysis shows that TOFs of methanol are determined by several factors: (a) the rate constants of the rate-limiting steps, (b) the coverages of the reactants and the products of the rate-limiting steps, and (c) the amount of free surfaces. These factors for CO and CO_2 hydrogenation are summarized in Table 3.

Based on Table 3, we explain why PBE and HSE give similar TOFs for the CO pathway. We only focus on r^+_{CO}, since $r^+_{\mathrm{CO}} \gg r^-_{\mathrm{CO}}$ for both PBE and HSE. This is because $K_{\mathrm{P,CO}}$ is much smaller than $K_{\mathrm{R,CO}}$ as shown in Table 3. The small $K_{\mathrm{P,CO}}$ is due to the fact that the Gibbs energy of the products (H_2(g) + H_2CO*) is much higher than the Gibbs energy of the reactants (H_3COH(g) + *), as observed in Fig. 2. The TOF of CO hydrogenation then becomes $R^{\mathrm{analytical}}_{\mathrm{CO}} \approx r^+_{\mathrm{CO}} = k_4^+ K_{\mathrm{R,CO}} \theta_*^2$. We now focus on $k_4^+ K_{\mathrm{R,CO}}$, which is determined by the Gibbs energy difference between CO(g)+H_2(g)+* and H-HCO*, that is, $k_4^+ K_{\mathrm{R,CO}} = \frac{k_B T}{h} e^{-\Delta G_R / k_B T}$, with $\Delta G_R = G_{\mathrm{H-HCO*}} - G_{\mathrm{CO}(g)} - G_{\mathrm{H_2}(g)} - G_*$. $G_{\mathrm{H-HCO*}}$ and G_* are the Gibbs energies of H-HCO* and Cu(211) surface, respectively. Fig. 2 shows that HSE gives a much larger ΔG_R than PBE, and therefore predicts a much smaller $k_4^+ K_{\mathrm{R,CO}}$. On the other hand, the HSE prediction for the free surface θ_* is about two orders of magnitude larger than the prediction from PBE, because PBE predicts that CO* nearly occupies the entire surface (due to PBE's overestimation of the binding energy between CO and copper). These effects cancel out, and finally PBE and HSE predicts similar TOFs for the CO hydrogenation.

Above discussions indicate that methanol's TOF also largely depends on the amount of free surface; therefore, we need to correctly predict the dominating adsorbates on copper. However, this is a challenging task for DFT. As we observed in Fig. 3, the prediction of dominating adsorbates much depends on the choice of XC functional. PBE and HSE predict CO* to be dominating on surface, while RPA predicts that both CO* and H* are dominating adsorbates.

We now explain why RPA TOF is much smaller than PBE TOF for CO hydrogenation (Table 2). Even though RPA predicts much larger free surface than PBE as shown in Table 3; however, RPA predicts much smaller k_4^+ and $K_{R,CO}$. The reason is that RPA gives a higher

Table 3: Equilibrium constants ($K_{\mathrm{R,CO}}$, $K_{\mathrm{R,CO_2}}$, $K_{\mathrm{P,CO}}$, and $K_{\mathrm{P,CO_2}}$), the amount of free surfaces (θ_*), and the forward and reverse rate constants (k_4^+, k_4^-, k_5^+, and k_5^-, in s^{-1}) of the rate-limiting steps from PBE, ONIOM(HSE:PBE), and ONIOM(RPA:PBE) calculations.

CO hydrogenation	k_4^+	k_4^-	θ_*	$K_{\mathrm{R,CO}}$	$K_{\mathrm{P,CO}}$
PBE	1.86×10^6	1.61×10^5	4.60×10^{-4}	4.71×10^{-5}	5.72×10^{-10}
HSE	3.98×10^4	2.01×10^3	4.98×10^{-2}	1.40×10^{-7}	3.95×10^{-14}
RPA	3.35×10^4	5.44×10^3	0.53	1.89×10^{-10}	2.62×10^{-10}
CO_2 hydrogenation	k_5^+	k_5^-	θ_*	$K_{\mathrm{R,CO_2}}$	$K_{\mathrm{P,CO_2}}$
PBE	4.90×10^2	1.91×10^5	0.30	3.96×10^{-7}	5.88×10^{-11}
HSE	2.57×10^1	2.15×10^3	0.22	3.06×10^{-6}	3.31×10^{-13}
RPA	8.25	10.52	0.39	3.14×10^{-8}	6.33×10^{-10}

forward reaction barrier for the rate-limiting step and a higher free energy for H*+HCO* (Fig. 2(a)). For CO_2 pathway, RPA predicts a TOF that is about three orders of magnitude slower than PBE. The reasons are two-fold: (a) PBE and RPA predict similar amount of free surface, and (b) RPA gives much smaller k_5^+ and K_{R,CO_2} as seen in Table 3.

3.5 Kinetics of methanol synthesis based on coupled CO and CO_2 hydrogenations

To investigate the competition between CO and CO_2 hydrogenation, we couple them through their common intermediates: H_2CO*, H*, H_3CO*, and H_3COH*. The conversion between CO_2 and CO is via the formation and decomposition of HCOOH*. To show that the choice of XC functional has a large impact on predicting the carbon source, we compute the consumption rates of CO and CO_2

$$T_{\mathrm{CO}} = k_3^+ \theta_{\mathrm{CO}} \theta_{\mathrm{H}} - k_3^- \theta_{\mathrm{HCO}} \theta_* \tag{11}$$

$$T_{\mathrm{CO_2}} = k_9^+ \theta_{\mathrm{CO_2}} \theta_{\mathrm{H}} - k_9^- \theta_{\mathrm{HCOO}} \theta_*. \tag{12}$$

The sum of T_{CO} and $T_{\mathrm{CO_2}}$ is equal to methanol's TOF (R). The fractional contribution from CO and CO_2 is defined as T_{CO}/R and $T_{\mathrm{CO_2}}/R$, respectively.

PBE, HSE, and RPA all predict HCO* + H* $\rightarrow$ H_2CO* + * to be the rate-limiting steps,

with X_{RC} being 0.996, 0.977, and 0.950, respectively. In Table 4, PBE predicts that nearly 100% methanol is produced from CO, while HSE and RPA increase the consumption rate of CO_2 to 1.37% and 4.88%, respectively. The increase of CO_2's consumption rate is largely due to the rapid decrease of the Gibbs energy difference (ΔG_{RLS}) between H-HCO* and H-HCOOH*, which are the rate-limiting steps of the CO and CO_2 hydrogenation pathways. We address that it is still an open question that what ΔG_{RLS} is by using more accurate XC functionals.

Table 4: Turnover frequencies (in s^{-1}) of methanol from microkinetic modeling with combined CO and CO_2 hydrogenations based on the Gibbs energies from PBE, ONIOM(HSE:PBE), and ONIOM(RPA:PBE) calculations. The fractional contributions of CO and CO_2 are shown. ΔG_{RLS} (in eV) is the Gibbs energy difference between H-HCO* and H-HCOOH*.

	PBE	HSE	RPA
methanol TOF	1.84×10^{-5}	1.21×10^{-5}	5.93×10^{-7}
CO%	100.01%	98.63%	95.12%
CO_2%	-0.01%	1.37%	4.88%
ΔG_{RLS}	0.56	0.22	0.14

Fig. 4 shows that the coverages of intermediates strongly depend on the choice of XC functionals. PBE and HSE predict that CO* is the major intermediate on surface, since they predict CO* to have the lowest Gibbs energy among all the intermediates before the rate-limiting step. On the other hand, RPA predicts HCOO* to be the major intermediate. PBE predicts nearly no free surface, while RPA predicts 34% free surface.

3.6 Assess RPA's accuracy for predicting the kinetics of CO and CO_2 hydrogenation

The accuracy of RPA is estimated by calculating the adsorption enthalpies of H, bidentate formate $HCOO_b$, HCOOH, H_2CO, and OH on Pt(111) using PBE, ONIOM(HSE:PBE), and ONIOM(RPA:PBE). We choose these systems for two reasons: (a) they are related to the intermediates in CO and CO_2 hydrogenation, except that the surface is Pt(111) rather than

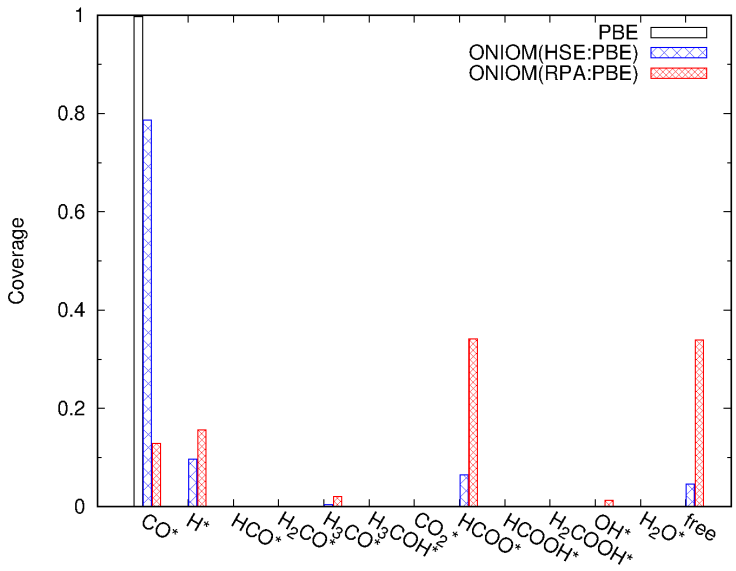

Figure 4: Coverages of the intermediates and the free surface from solving the microkinetic models with the coupled CO and CO_2 hydrogenation, based on the energies from PBE, ONIOM(HSE:PBE), and ONIOM(RPA:PBE) calculations. The amount of free surface is denoted by "free".

Cu(211), and (b) experiment results exist. The results are given in Fig. 5. To be consistent with Fig. 2, the enthalpy of H_2CO^* is referenced to gas-phase CO and H_2 at 1 atm and 298.15 K. For systems containing two oxygen atoms, their enthalpies are referenced to CO_2 and H_2 at 1 atm and 298.15 K.

We discuss how the experiment results in Fig. 5 are estimated. For H_2CO^*, it is estimated based on the measured activation energy (0.57 eV) for its desorption from Pt(111).[112] The desorption is barrierless based on our NEB calculations; therefore, we take this desorption barrier as the adsorption energy. The thermal corrections to H_2CO^*, CO(g), H_2(g), and H_2CO(g) are calculated using DFT. The formation enthalpy of H_2CO/Pt(111) is estimated to be 0.35 eV, referenced to CO(g), H_2(g), and Pt(111). For OH/Pt(111) and H/Pt(111), their experiment formation enthalpies are -0.37 eV and -1.75 eV, respectively.[113] They are referenced to O_2(g) and H_2(g). We change the references to CO(g), CO_2(g), and H_2(g) by computing the reaction enthalpy of $CO + 1/2O_2 \rightarrow CO_2$, which is determined to be -2.93 eV based on the standard formation enthalpies of CO (-1.14 eV)[94] and CO_2 (-4.07 eV)[94] taken

from NIST Chemistry WebBook. The experiment formation enthalpy of $HCOO_b$/Pt(111) is $-(410-74\theta)$ kJ/mol, where θ is $HCOO_b$'s coverage.[114] By setting $\theta = 1/9$ (the coverage in our DFT calculations), the formation enthalpy of $HCOO_b$/Pt(111) is -4.16 eV. Based on the formation enthalpy of CO_2 (-4.07 eV),[94] the enthalpy of $HCOO_b$/Pt(111) is -0.09 eV, referenced to CO_2(g), H_2(g), and Pt(111). The experiment adsorption enthalpy of HCOOH/Pt(111) at 0.25 monolayer is -0.65 eV.[114] With the formation enthalpy of HCOOH(g) (-3.92 eV),[115] the enthalpy of HCOOH/Pt(111) is -0.49 eV, referenced to CO_2(g), H_2(g), and Pt(111).

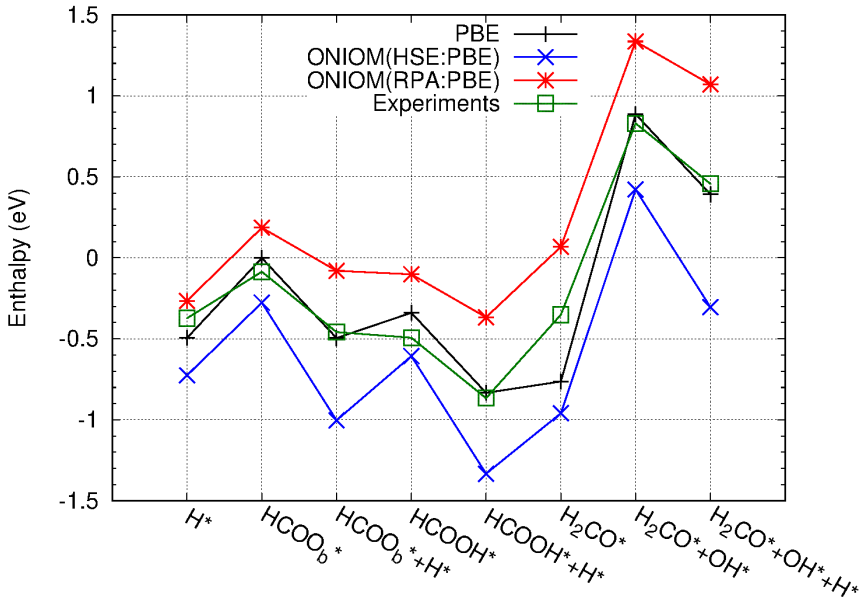

Figure 5: Enthalpies of selected molecules and radicals adsorbed on Pt(111), from PBE, ONIOM(HSE:PBE), ONIOM(RPA:PBE) calculations. The DFT results are compared to the experiment results. For adsorbates containing two oxygen atoms, the enthalpies are referenced to CO_2(g) and H_2(g). For adsorbates containing one oxygen atom, the enthalpies are referenced to CO(g) and H_2(g).

Fig. 5 shows that the PBE results agree well with the experiment results, except for H_2CO*. The HSE results deviate significantly from the experiment results, which casts doubts on employing HSE functional to investigate methanol synthesis. The RPA results are consistently higher than the experiment results.

To understand the errors of RPA, let's take HCOOH/Pt(111) as an example. We note that the RPA prediction for the reaction enthalpy of CO_2(g)+H_2(g) $\rightarrow$ HCOOH(g) at the

standard conditions is 0.13 eV, which agrees well with the experiment value 0.16 eV. Therefore, the reason for RPA's underestimation of the enthalpies of HCOOH/Pt(111) is due to its underestimation of the binding energy between HCOOH and Pt(111). This is a known shortcoming of RPA: RPA tends to underestimate binding energies.[68,116–118] We also perform a similar analysis on H_2CO/Pt(111). The RPA reaction enthalpy of CO(g)+H_2(g) $\rightarrow$ H_2CO(g) at the standard conditions is 0.13 eV higher than the experiment value. Fig. 5 shows that RPA underestimates the enthalpy of H_2CO/Pt(111) by 0.42 eV. Combining these two, RPA underestimates the binding energy between H_2CO and Pt(111) by 0.29 eV ($= 0.42 - 0.13$). This, again, is due to the underbinding problem of RPA.

The above mentioned errors of RPA bring up the question: How much can we trust the RPA predictions for the kinetics of methanol synthesis? Another question is that, since PBE gives good predictions to all adsorbates except H_2CO/Pt(111), shall we trust the kinetics of methanol synthesis predicted by PBE? The key difference between the RPA and PBE predictions is whether CO_2 contributes to the methanol synthesis on copper, which largely depends on the relative energy between the transition states H-HCO/Cu(211) and H-HCOOH/Cu(211). Therefore, in the following we focus on the energies of HCOOH+H/Pt(111) and H_2CO/Pt(111) which are the reactant and product associated with these two transition states, except that the surface is Pt(111) rather than Cu(211).

The following discussions are based on the assumption that the errors of PBE and RPA in predicting the energies of H_2CO/Pt(111) and H+HCOOH/Pt(111) are similar with their errors for predicting the energies of H-HCO/Cu(211) and H-HCOOH/Cu(211). Fig. 5 shows that PBE has no error cancellation between H+HCOOH/Pt(111) and H_2CO/Pt(111). PBE gives an accurate prediction to H+HCOOH/Pt(111); however, the PBE prediction for H_2CO/Pt(111) is -0.41 eV lower than the experiment. In Fig. 2, PBE predicts that the Gibbs energy of H-HCOOH/Cu(211) is 0.56 eV higher than H-HCO/Cu(211) after the correction. With the above assumption, we correct the PBE energies, and find that HCOOH-H/Cu(211) is only 0.12 eV ($= 0.56 - 0.41$) higher than H-HCO/Cu(111). The corrected PBE results

suggest that CO_2 hydrogenation is competitive.

On the other hand, Fig. 5 shows that RPA has a good error cancellation between HCOOH+H/Pt(111) and H_2CO/Pt(111): the RPA errors for HCOOH-H/Pt(111) and H_2CO/Pt(111) are 0.49 eV and 0.41 eV, respectively. In Fig. 2, RPA predicts that the Gibbs energy of H-HCOOH/Cu(211) is 0.14 eV higher than H-HCO/Cu(211). Again, with the above assumption, we can correct the RPA energies, and find that H-HCOOH/Cu(211) is only 0.06 eV higher than H-HCO/Cu(211) after the correction. The corrected RPA results still suggest that CO_2 hydrogenation is competitive for methanol synthesis over Cu(211).

4 Conclusions

In this work, we investigated different types of XC functionals for predicting the thermodynamics and kinetics of methanol synthesis over copper. We showed that the kinetics of methanol synthesis strongly depends on the choice of XC functionals, due to the presence of competing reaction pathways (i.e., CO and CO_2 hydrogenations). PBE predicted that the surface is almost fully occupied by CO with nearly no free surface left, while RPA predicted that the surface is largely occupied by formate with a large amount (34%) of free surface. It is found that the turnover frequencies of methanol do not only depend on the overall barriers of the reactions, but also depend on the amount of free surface. PBE predicted that CO is the carbon source, which contradicts the previous isotope-labeling experiments that suggested CO_2 as the carbon source. PBE results, therefore, suggest that metallic copper is not the active site for CO_2 hydrogenation in industrial methanol synthesis. A different picture is given by RPA. RPA predicted that CO_2 hydrogenation is also competitive, therefore suggesting that metallic copper is still a possible active site for catalyzing CO_2 hydrogenation. We note that the reaction networks employed in this work is rather simplified; therefore, future modeling using more comprehensive reaction networks is required to resolve the mechanism of methanol synthesis on copper.

We examined the accuracy of RPA by computing the adsorption energies of selected molecules and radicals on Pt(111). We focused on the enthalpies of HCOOH+H/Pt(111) and H_2CO/Pt(111), which are closely related to the rate-limiting steps in methanol synthesis, except that the substrate is Pt(111) rather than Cu(211). Their enthalpies predicted by RPA are consistently higher than the benchmarks, which is attributed to RPA's underestimation of binding energies. Nevertheless, RPA has a good error cancellation between HCOOH+H/Pt(111) and H_2CO/Pt(111). By assuming that the similar error cancellation exists for H-HCO/Cu(211) and H-HCOOH/Cu(211), RPA's prediction that CO_2 hydrogenation is completive may be true. However, we address that it is still an open question that whether copper is the active site for catalyzing CO_2 hydrogenation in industrial methanol synthesis. To answer this question, further development of accurate and computationally efficient XC functional is required.

Supporting Information Available

Details of the rate equations for microkinetic modeling. This material is available free of charge via the Internet at http://pubs.acs.org.

Acknowledgement

This work is supported by the Florida State University (start-up fund) and National Science Foundation under CHE-1752769.

References

(1) Waugh, K. Methanol Synthesis. *Catal. Today* **1992**, *15*, 51 – 75.

(2) Hansen, P. L.; Wagner, J. B.; Helveg, S.; Rostrup-Nielsen, J. R.; Clausen, B. S.;

Topsøe, H. Atom-resolved imaging of dynamic shape changes in supported copper nanocrystals. *Science* **2002**, *295*, 2053–2055.

(3) Bart, J.; Sneeden, R. Copper-zinc oxide-alumina methanol catalysts revisited. *Catal. Today* **1987**, *2*, 1 – 124.

(4) Chinchen, G.; Waugh, K.; Whan, D. The activity and state of the copper surface in methanol synthesis catalysts. *Appl. Catal.* **1986**, *25*, 101 – 107.

(5) Chinchen, G.; Denny, P.; Jennings, J.; Spencer, M.; Waugh, K. Synthesis of methanol. *Appl. Catal.* **1988**, *36*, 1 – 65.

(6) Pan, W.; Cao, R.; Roberts, D.; Griffin, G. Methanol synthesis activity of CuZnO catalysts. *J. Catal* **1988**, *114*, 440 – 446.

(7) Burch, R.; Golunski, S. E.; Spencer, M. S. The role of copper and zinc oxide in methanol synthesis catalysts. *J. Chem. Soc., Faraday Trans.* **1990**, *86*, 2683–2691.

(8) Burch, R.; Golunski, S. E.; Spencer, M. S. The role of hydrogen in methanol synthesis over copper catalysts. *Catal. Lett.* **1990**, *5*, 55–60.

(9) Rasmussen, P.; Kazuta, M.; Chorkendorff, I. Synthesis of methanol from a mixture of H_2 and CO_2 on Cu(100). *Surf. Sci.* **1994**, *318*, 267 – 280.

(10) Yoshihara, J.; Parker, S. C.; Schafer, A.; Campbell, C. T. Methanol synthesis and reverse water-gas shift kinetics over clean polycrystalline copper. *Catal. Lett.* **1995**, *31*, 313–324.

(11) Ovesen, C.; Clausen, B.; Schiøtz, J.; Stoltze, P.; Topsøe, H.; Nørskov, J. K. Kinetic implications of dynamical changes in catalyst morphology during methanol synthesis over Cu/ZnO catalysts. *Journal of Catalysis* **1997**, *168*, 133–142.

(12) Jun, K.-W.; Shen, W.-J.; Rao, K. R.; Lee, K.-W. Residual sodium effect on the catalytic activity of $Cu/ZnO/Al_2O_3$ in methanol synthesis from CO_2 hydrogenation. *Appl. Catal., A* **1998**, *174*, 231 – 238.

(13) Twigg, M. V.; Spencer, M. S. Deactivation of supported copper metal catalysts for hydrogenation reactions. *Appl. Catal., A* **2001**, *212*, 161 – 174.

(14) Hong, Z. S.; Cao, Y.; Deng, J. F.; Fan, K. N. CO_2 hydrogenation to methanol over $Cu/ZnO/Al_2O_3$ catalysts prepared by a novel gel-network-coprecipitation method. *Catal. Lett.* **2002**, *82*, 37–44.

(15) Baltes, C.; Vukojević, S.; Schüth, F. Correlations between synthesis, precursor, and catalyst structure and activity of a large set of $CuO/ZnO/Al_2O_3$ catalysts for methanol synthesis. *J. Catal.* **2008**, *258*, 334–344.

(16) Lim, H. W.; Park, M. J.; Kang, S. H.; Chae, H. J.; Bae, J. W.; Jun, K. W. Modeling of the kinetics for methanol synthesis using $Cu/ZnO/Al_2O_3/ZrO_2$ catalyst: influence of carbon dioxide during hydrogenation. *Ind. Eng. Chem. Res.* **2009**, *48*, 10448–10455.

(17) Yang, Y.; Evans, J.; Rodriguez, J. A.; White, M. G.; Liu, P. Fundamental studies of methanol synthesis from CO_2 hydrogenation on Cu (111), Cu clusters, and Cu/ZnO(0001). *Phys. Chem. Chem. Phys.* **2010**, *12*, 9909–9917.

(18) Inui, T.; Hara, H.; Takeguchi, T.; Kim, J.-B. Structure and function of Cu-based composite catalysts for highly effective synthesis of methanol by hydrogenation of CO_2 and CO. *Catal. Today* **1997**, *36*, 25 – 32.

(19) Toyir, J.; de la Piscina, P. R.; Fierro, J. L. G.; Homs, N. Highly effective conversion of CO_2 to methanol over supported and promoted copper-based catalysts: influence of support and promoter. *Appl. Catal., B* **2001**, *29*, 207–215.

(20) Słoczyński, J.; Grabowski, R.; Olszewski, P.; Kozłowska, A.; Stoch, J.; Lachowska, M.; Skrzypek, J. Effect of metal oxide additives on the activity and stability of $Cu/ZnO/ZrO_2$ catalysts in the synthesis of methanol from CO_2 and H_2. *Appl. Catal., A* **2006**, *310*, 127–137.

(21) Clancy, P.; Breen, J. P.; Ross, J. R. The preparation and properties of coprecipitated Cu-Zr-Y and Cu-Zr-La catalysts used for the steam reforming of methanol. *Catal. Today* **2007**, *127*, 291 – 294.

(22) Millar, G. J.; Rochester, C. H.; Waugh, K. C. Evidence for the adsorption of molecules at special sites located at copper/zinc oxide interfaces. Part 3.-Fourier-transform infrared study of methyl formate adsorption on reduced and oxidised $Cu/ZnO/SiO_2$ catalysts. *J. Chem. Soc., Faraday Trans.* **1992**, *88*, 3497–3503.

(23) Bussche, K. V.; Froment, G. Nature of formate in methanol synthesis on $Cu/ZnO/Al_2O_3$. *Appl. Catal., A* **1994**, *112*, 37 – 55.

(24) Bailie, J. E.; Rochester, C. H.; Millar, G. J. Spectroscopic evidence for adsorption sites located at Cu/ZnO interfaces. *Catal. Lett.* **1995**, *31*, 333–340.

(25) Poels, E.; Brands, D. Modification of $Cu/ZnO/SiO_2$ catalysts by high temperature reduction. *Appl. Catal., A* **2000**, *191*, 83 – 96.

(26) Herman, R.; Klier, K.; Simmons, G.; Finn, B.; Bulko, J.; Kobylinski, T. Catalytic synthesis of methanol from COH_2: I. Phase composition, electronic properties, and activities of the $Cu/ZnO/M_2O_3$ catalysts. *J. Catal* **1979**, *56*, 407 – 429.

(27) Mehta, S.; Simmons, G.; Klier, K.; Herman, R. Catalytic synthesis of methanol from COH_2: II. Electron microscopy (TEM, STEM, microdiffraction, and energy dispersive analysis) of the CuZnO and $Cu/ZnO/Cr_2O_3$ catalysts. *J. Catal* **1979**, *57*, 339–360.

(28) Spencer, M. The role of zinc oxide in Cu/ZnO catalysts for methanol synthesis and the water-gas shift reaction. *Top. Catal* **1999**, *8*, 259–266.

(29) Fujitani, T.; Nakamura, I.; Uchijima, T.; Nakamura, J. The kinetics and mechanism of methanol synthesis by hydrogenation of CO_2 over a Zn-deposited Cu(111) surface. *Surf. Sci.* **1997**, *383*, 285 – 298.

(30) Klier, K.; Chatikavanij, V.; Herman, R.; Simmons, G. Catalytic synthesis of methanol from COH_2. *J. Catal* **1982**, *74*, 343 – 360.

(31) Klier, K. *Advances in Catalysis*; Elsevier, 1982; Vol. 31; pp 243–313.

(32) Lim, K. H.; Chen, Z. X.; Neyman, K. M.; Rösch, N. Comparative theoretical study of formaldehyde decomposition on PdZn, Cu, and Pd surfaces. *J. Phys. Chem. C* **2006**, *110*, 14890–14897.

(33) Tang, Q. L.; Hong, Q. J.; Liu, Z. P. CO_2 fixation into methanol at Cu/ZrO_2 interface from first principles kinetic Monte Carlo. *J. Catal* **2009**, *263*, 114 – 122.

(34) Chinchen, G.; Waugh, K. The chemical state of copper during methanol synthesis. *J. Catal* **1986**, *97*, 280 – 283.

(35) Baussart, H.; Delobel, R.; Bras, M. L.; Maguer, D. L.; Leroy, J.-M. A macroscopic study of Cu/Zn/Al catalyst for carbon dioxide hydrogenation. *Appl. Catal.* **1985**, *14*, 381 – 389.

(36) Vedage, G. A.; Himelfarb, P. B.; Simmons, G. W.; Klier, K. *Solid State Chemistry in Catalysis*; Chapter 19, pp 295–312.

(37) Graaf, G.; Stamhuis, E.; Beenackers, A. Kinetics of low-pressure methanol synthesis. *Chem. Eng. Sci.* **1988**, *43*, 3185 – 3195.

(38) Calverley, E. M.; Smith, K. J. Kinetic model for alcohol synthesis over a promoted copper/zinc oxide/chromium oxide (Cr_2O_3) catalyst. *Ind. Eng. Chem. Res.* **1992**, *31*, 792–803.

(39) Grabow, L. C.; Mavrikakis, M. Mechanism of methanol synthesis on Cu through CO_2 and CO hydrogenation. *ACS Catalysis* **2011**, *1*, 365–384.

(40) Liu, G.; Willcox, D.; Garland, M.; Kung, H. The role of CO_2 in methanol synthesis on Cu/Zn oxide: An isotope labeling study. *J. Catal* **1985**, *96*, 251 – 260.

(41) Denise, B.; Sneeden, R.; Beguin, B.; Cherifi, O. Supported copper catalysts in the synthesis of methanol: N_2O-titrations. *Appl. Catal.* **1987**, *30*, 353 – 363.

(42) Jackson, S. D. Isotopic exchange of carbon dioxide and its interaction with carbon monoxide over copper catalysts. *J. Catal* **1989**, *115*, 247 – 249.

(43) Denise, B.; Sneeden, R.; Hamon, C. Hydrocondensation of carbon dioxide: IV. *J. Mol. Catal.* **1982**, *17*, 359 – 366.

(44) Chinchen, G.; Denny, P.; Parker, D.; Spencer, M.; Whan, D. Mechanism of methanol synthesis from $CO_2/CO/H_2$ mixtures over copper/zinc oxide/alumina catalysts: use of 14C-labelled reactants. *Appl. Catal.* **1987**, *30*, 333 – 338.

(45) Takagawa, M.; Ohsugi, M. Study on reaction rates for methanol synthesis from carbon monoxide, carbon dioxide, and hydrogen. *J. Catal* **1987**, *107*, 161 – 172.

(46) Hansen, J. B.; Højlund Nielsen, P. E. In *Handbook of Heterogeneous Catalysis*; Ertl, G., Knözinger, H., Schüth, F., Weitkamp, J., Eds.; Wiley-VCH Verlag GmbH & Co. KGaA, 2008.

(47) Studt, F.; Behrens, M.; Kunkes, E. L.; Thomas, N.; Zander, S.; Tarasov, A.; Schumann, J.; Frei, E.; Varley, J. B.; Abild-Pedersen, F. et al. The mechanism of CO

and CO_2 hydrogenation to methanol over Cu-based catalysts. *ChemCatChem* **2015**, *7*, 1105–1111.

(48) Sun, Q.; Liu, C. W.; Pan, W.; Zhu, Q. M.; Deng, J. F. In situ IR studies on the mechanism of methanol synthesis over an ultrafine $Cu/ZnO/Al_2O_3$ catalyst. *Appl Catal., A* **1998**, *171*, 301 – 308.

(49) Sun, Q. On the catalytic mechanism of $Cu/ZnO/Al_2O_3$ for CO_x hydrogenation. Natural Gas Conversion VII: Proceedings of the 7th Natural Gas Conversion Symposium. Dalian, China, June 2004.

(50) Kagan, Y. B.; Liberov, L. G.; Slivinski, E. V.; Lotkev, S. M.; Liu, G. I.; Rozovskii, A. Y.; Bashkirov, A. N. *Dokl. Akad. Nauk. SSSR* **1975**, *221*, 1093.

(51) Chinchen, G.; Denny, P.; Parker, D.; Short, D.; Spencer, M.; Waugh, K.; Whan, D. *Prepr. Amer. Chem. Soc. Div. Fuel Chem.* **1984**, *29*, 178.

(52) Hohenberg, P.; Kohn, W. Inhomogeneous electron gas. *Phys. Rev.* **1964**, *136*, B864–B871.

(53) Kohn, W.; Sham, L. J. Self-consistent equations including exchange and correlation effects. *Phys. Rev.* **1965**, *140*, A1133–A1138.

(54) Hammer, B.; Hansen, L. B.; Nørskov, J. K. Improved adsorption energetics within density-functional theory using revised Perdew-Burke-Ernzerhof functionals. *Phys. Rev. B* **1999**, *59*, 7413–7421.

(55) Feibelman, P. J.; Hammer, B.; Nørskov, J. K.; Wagner, F.; Scheffler, M.; Stumpf, R.; Watwe, R.; Dumesic, J. The CO/Pt (111) puzzle. *J. Phys. Chem. B* **2001**, *105*, 4018–4025.

(56) Behrens, M.; Studt, F.; Kasatkin, I.; Kühl, S.; Hävecker, M.; Abild-Pedersen, F.;

Zander, S.; Girgsdies, F.; Kurr, P.; Kniep, B.-L. et al. The active site of methanol synthesis over $Cu/ZnO/Al_2O_3$ industrial catalysts. *Science* **2012**, *336*, 893–897.

(57) Studt, F.; Abild-Pedersen, F.; Varley, J. B.; Nørskov, J. K. CO and CO_2 hydrogenation to methanol calculated using the BEEF-vdW functional. *Catal. Lett.* **2013**, *143*, 71–73.

(58) Wellendorff, J.; Lundgaard, K. T.; Møgelhøj, A.; Petzold, V.; Landis, D. D.; Nørskov, J. K.; Bligaard, T.; Jacobsen, K. W. Density functionals for surface science: Exchange-correlation model development with Bayesian error estimation. *Phys. Rev. B* **2012**, *85*, 235149.

(59) Van Rensburg, W. J.; Petersen, M. A.; Datt, M. S.; den Berg, J.-A.; Helden, P. On the kinetic interpretation of DFT-derived energy profiles: Cu-catalyzed methanol synthesis. *Catal. Lett.* **2015**, *2*, 559–568.

(60) Peterson, A. A.; Abild-Pedersen, F.; Studt, F.; Rossmeisl, J.; Nørskov, J. K. How copper catalyzes the electroreduction of carbon dioxide into hydrocarbon fuels. *Energy Environ. Sci.* **2010**, *3*, 1311–1315.

(61) Bohm, D.; Pines, D. A collective description of electron interactions. I. magnetic Interactions. *Phys. Rev.* **1951**, *82*, 625–634.

(62) McLachlan, A. D.; Ball, M. A. Time-dependent Hartree-Fock theory for molecules. *Rev. Mod. Phys.* **1964**, *36*, 844–855.

(63) Langreth, D. C.; Perdew, J. P. The exchange-correlation energy of a metallic surface. *Solid State Commun.* **1975**, *17*, 1425–1429.

(64) Gunnarsson, O.; Lundqvist, B. I. Exchange and correlation in atoms, molecules, and solids by the spin-density-functional formalism. *Phys. Rev. B* **1976**, *13*, 4274–4298.

(65) Langreth, D. C.; Perdew, J. P. Exchange-correlation energy of a metallic surface wave-vector analysis. *Phys. Rev. B* **1977**, *15*, 2884.

(66) Andersson, Y.; Langreth, D. C.; Lundqvist, B. I. van der Waals interactions in density-functional theory. *Phys. Rev. Lett.* **1996**, *76*, 102–105.

(67) Dobson, J. F.; Wang, J. Successful test of a seamless van der Waals density functional. *Phys. Rev. Lett.* **1999**, *82*, 2123–2126.

(68) Furche, F. Molecular tests of the random phase approximation to the exchange-correlation energy functional. *Phys. Rev. B* **2001**, *64*, 195120.

(69) Schimka, L.; Harl, J.; Stroppa, A.; Grüneis, A.; Marsman, M.; Mittendorfer, F.; Kresse, G. Accurate surface and adsorption energies from many-body perturbation theory. *Nature Materials* **2010**, *9*, 741–744.

(70) Karlický, František and Lazar, Petr and Dubecký, Matuš and Otyepka, Michal, Random phase approximation in surface chemistry: Water splitting on iron. *J. Chem. Theory Comput.* **2013**, *9*, 3670–3676.

(71) Bao, J. L.; Yu, H. S.; Duanmu, K.; Makeev, M. A.; Xu, X.; Truhlar, D. G. Density functional theory of the water splitting reaction on Fe(0): comparison of local and nonlocal correlation functionals. *ACS Catalysis* **2015**, *5*, 2070–2080.

(72) Perdew, J. P.; Burke, K.; Ernzerhof, M. Generalized gradient approximation made simple. *Phys. Rev. Lett.* **1996**, *77*, 3865.

(73) Heyd, J.; Scuseria, G. E.; Ernzerhof, M. Hybrid functionals based on a screened Coulomb potential. *J. Chem. Phys.* **2003**, *118*, 8207–8215.

(74) Krukau, A. V.; Vydrov, O. A.; Izmaylov, A. F.; Scuseria, G. E. Influence of the exchange screening parameter on the performance of screened hybrid functionals. *The Journal of Chemical Physics* **2006**, *125*, 224106.

(75) Dumesic, J. A.; Rudd, D. F.; Aparicio, L. M.; Rekoske, J. E.; Treviño, A. A. *The microkinetics of heterogeneous catalysis*; ACS Professional Reference Book, American Chemical Society, Washington, DC, 1993; p 315.

(76) Frisch, M. J.; Trucks, G. W.; Schlegel, H. B.; Scuseria, G. E.; Robb, M. A.; Cheeseman, J. R.; Scalmani, G.; Barone, V.; Petersson, G. A.; Nakatsuji, H. et al. Gaussian 09 Revision E.01. Gaussian Inc. Wallingford CT 2009.

(77) Perdew, J. P.; Wang, Y. Accurate and simple analytic representation of the electron-gas correlation energy. *Physical Review B* **1992**, *45*, 13244–13249.

(78) Verma, P.; Truhlar, D. G. HLE16: A local Kohn-Sham gradient approximation with good performance for semiconductor band gaps and molecular excitation energies. *The Journal of Physical Chemistry Letters* **2017**, *8*, 380–387.

(79) Tao, J.; Perdew, J. P.; Staroverov, V. N.; Scuseria, G. E. Climbing the density functional ladder: nonempirical meta–generalized gradient approximation designed for molecules and solids. *Physical Review Letters* **2003**, *91*, 146401.

(80) Perdew, J. P.; Ruzsinszky, A.; Csonka, G. I.; Constantin, L. A.; Sun, J. Workhorse semilocal density functional for condensed matter physics and quantum chemistry. *Physical Review Letters* **2009**, *103*, 026403.

(81) Perdew, J. P.; Ruzsinszky, A.; Csonka, G. I.; Constantin, L. A.; Sun, J. Erratum: workhorse semilocal density functional for condensed matter physics and quantum chemistry [Phys. Rev. Lett.103, 026403 (2009)]. *Physical Review Letters* **2011**, *106*, 179902.

(82) Sun, J.; Ruzsinszky, A.; Perdew, J. Strongly constrained and appropriately normed semilocal density functional. *Physical Review Letters* **2015**, *115*, 036402.

(83) Verma, P.; Truhlar, D. G. HLE17: An improved local exchange-correlation functional for computing semiconductor band gaps and molecular excitation energies. *The Journal of Physical Chemistry C* **2017**, *121*, 7144–7154.

(84) Zhao, Y.; Truhlar, D. G. A new local density functional for main-group thermochemistry, transition metal bonding, thermochemical kinetics, and noncovalent interactions. *The Journal of Chemical Physics* **2006**, *125*, 194101.

(85) Perdew, J. P.; Ernzerhof, M.; Burke, K. Rationale for mixing exact exchange with density functional approximations. *The Journal of Chemical Physics* **1996**, *105*, 9982–9985.

(86) Becke, A. D. Density-functional thermochemistry. III. The role of exact exchange. *The Journal of Chemical Physics* **1993**, *98*, 5648–5652.

(87) Kresse, G.; Hafner, J. Ab initio molecular dynamics for liquid metals. *Phys. Rev. B* **1993**, *47*, 558.

(88) Kresse, G.; Hafner, J. Ab initio molecular-dynamics simulation of the liquid-metal–amorphous-semiconductor transition in germanium. *Phys. Rev. B* **1994**, *49*, 14251.

(89) Kresse, G.; Furthmüller, J. Efficiency of ab-initio total energy calculations for metals and semiconductors using a plane-wave basis set. *Comput. Mater. Sci.* **1996**, *6*, 15–50.

(90) Kresse, G.; Furthmüller, J. Efficient iterative schemes for ab initio total-energy calculations using a plane-wave basis set. *Phys. Rev. B* **1996**, *54*, 11169.

(91) Kresse, G.; Joubert, D. From ultrasoft pseudopotentials to the projector augmented-wave method. *Phys. Rev. B* **1999**, *59*, 1758.

(92) Dunning Jr, T. H. Gaussian basis sets for use in correlated molecular calculations. I. The atoms boron through neon and hydrogen. *J. Chem. Phys.* **1989**, *90*, 1007–1023.

(93) Linstrom, P., Mallard, W., Eds. *NIST Chemistry WebBook, NIST Standard Reference Database Number 69*; National Institute of Standards and Technology, Gaithersburg MD, 20899, retrieved January 16, 2018.

(94) Cox, J.; Wagman, D.; Medvedev, V. *CODATA Key Values for Thermodynamics*; Hemisphere Publishing Corp., New York, 1984.

(95) Giannozzi, P.; Baroni, S.; Bonini, N.; Calandra, M.; Car, R.; Cavazzoni, C.; Ceresoli, D.; Chiarotti, G. L.; Cococcioni, M.; Dabo, I. et al. QUANTUM ESPRESSO: a modular and open-source software project for quantum simulations of materials. *J. Phys. Condens. Matter* **2009**, *21*, 395502.

(96) Monkhorst, H. J.; Pack, J. D. Special points for Brillouin-zone integrations. *Phys. Rev. B* **1976**, *13*, 5188.

(97) Weinan, E.; Ren, W.; Vanden-Eijnden, E. String method for the study of rare events. *Phys. Rev. B* **2002**, *66*, 052301.

(98) Weinan, E.; Ren, W.; Vanden-Eijnden, E. Simplified and improved string method for computing the minimum energy paths in barrier-crossing events. *J. Chem. Phys.* **2007**,

(99) Mills, G.; Jónsson, H. Quantum and thermal effects in H_2 dissociative adsorption: Evaluation of free energy barriers in multidimensional quantum systems. *Phys. Rev. Lett.* **1994**, *72*, 1124–1127.

(100) Mills, G.; Jónsson, H.; Schenter, G. K. Reversible work transition state theory: Application to dissociative adsorption of hydrogen. *Surf. Sci.* **1995**, *324*, 305 – 337.

(101) Jónsson, H.; Mills, G.; Jacobsen, K. W. *Classical and quantum dynamics in condensed phase simulations*; World Scientific, 1998; pp 385–404.

(102) Henkelman, G.; Uberuaga, B. P.; Jónsson, H. A climbing image nudged elastic band method for finding saddle points and minimum energy paths. *J. Chem. Phys.* **2000**, *113*, 9901–9904.

(103) Svensson, M.; Humbel, S.; Froese, R. D.; Matsubara, T.; Sieber, S.; Morokuma, K. ONIOM: A multilayered integrated MO+MM method for geometry optimizations and single point energy predictions. A test for Diels-Alder reactions and $Pt(P(t\text{-}Bu)_3)_2+H_2$ oxidative addition. *J. Phys. Chem.* **1996**, *100*, 19357–19363.

(104) Kaltak, M.; Klimeš, J.; Kresse, G. Low scaling algorithms for the random phase approximation: Imaginary time and Laplace transformations. *Journal of chemical theory and computation* **2014**, *10*, 2498–2507.

(105) Fowler, R.; Guggenheim, E. A. *Statistical Thermodynamics*; Cambridge Univ. Press, Cambridge, England, 1960.

(106) Stoltze, P.; Nørskov, J. Bridging the pressure gap between ultrahigh-vacuum surface physics and high-pressure catalysis. *Phys. Rev. Lett.* **1985**, *55*, 2502.

(107) MATLAB version R2017a. *The MathWorks, Inc., Natick, Massachusetts, United States.*

(108) Campbell, C. T. Finding the rate-determining step in a mechanism: comparing DeDonder relations with the âĂIJdegree of rate controlâĂİ. *J. Catal* **2001**, *204*, 520 – 524.

(109) Wellendorff, J.; Silbaugh, T. L.; Garcia-Pintos, D.; Nørskov, J. K.; Bligaard, T.; Studt, F.; Campbell, C. T. A benchmark database for adsorption bond energies to transition metal surfaces and comparison to selected DFT functionals. *Surf. Sci.* **2015**, *640*, 36 – 44, Reactivity Concepts at Surfaces: Coupling Theory with Experiment.

(110) Duanmu, K.; Truhlar, D. G. Validation of density functionals for adsorption energies on transition metal surfaces. *Journal of Chemical Theory and Computation* **2017**, *13*, 835–842.

(111) Stoltze, P. Surface science as the basis for the understanding of the catalytic synthesis of ammonia. *Phys. Scr.* **1987**, *36*, 824.

(112) Abbas, N. M.; Madix, R. J. The effects of structured overlayers of sulfur on the kinetics and mechanism of simple reactions on Pt (111): I. Formaldehyde decomposition. *Solid State Commun.* **1981**, *7*, 241–275.

(113) Karp, E. M.; Campbell, C. T.; Studt, F.; Abild-Pedersen, F.; Nørskov, J. K. Energetics of oxygen adatoms, hydroxyl species and water dissociation on Pt(111). *J. Phys. Chem. C* **2012**, *116*, 25772–25776.

(114) Silbaugh, T. L.; Karp, E. M.; Campbell, C. T. Energetics of formic acid conversion to adsorbed formates on Pt (111) by transient calorimetry. *J. Am. Chem. Soc.* **2014**, *136*, 3964–3971.

(115) Guthrie, J. P. Hydration of carboxamides. Evaluation of the free energy change for addition of water to acetamide and formamide derivatives. *J. Am. Chem. Soc.* **1974**, *96*, 3608–3615.

(116) Harl, J.; Kresse, G. Accurate bulk properties from approximate many-body techniques. *Phys. Rev. Lett.* **2009**, *103*, 056401.

(117) Ren, X.; Rinke, P.; Scheffler, M. Exploring the random phase approximation: Application to CO adsorbed on Cu (111). *Phys. Rev. B* **2009**, *80*, 045402.

(118) Harl, J.; Schimka, L.; Kresse, G. Assessing the quality of the random phase approximation for lattice constants and atomization energies of solids. *Phys. Rev. B* **2010**, *81*, 115126.

Graphical TOC Entry